Supplementary Material

Information here are presented in the order in which they are mentioned in the manuscript.

1 ADDITIONAL INFORMATION ON LABORATORY TESTS TO CALIBRATE THE DEM MODELS

Numerical calculations were based on laboratory experiments on concrete performed by (Van Vliet and Van Mier, 1999). Concrete with the following properties was used (see Tab.1): water-cement ratio $w/c = 0.5$, Portland cement type B 375kg, aggregates 2-8 mm in diameter - 903 kg and sand 0.125-2 mm in diameter - 905 kg). The average compressive strength of cubes was 50 MPa. The size and the shape of the specimen (dog-bone shape) were shown in Fig. (Van Vliet and Van Mier, 1999) (specimen "B": height - 150 mm, width - 100 mm and depth - 100 mm). The experimental force - deformation curve was shown in Fig.3 of (Van Vliet and Van Mier, 1999). The experimental nominal tensile strength was $f_t = 2.97$ MPa. The shape of the crack in the numerical calculation was similar to that in the experiment (Van Vliet and Van Mier, 1999).

The thickness of the concrete specimen in experiments was 100 mm. The physical model was three-dimensional. To shorten a computer effort related to a huge number of particles in 3D conditions, the numerical concrete specimen was 2D one, i.e. it solely included one layer of particles. The particles of different sizes were made of aggregate and mortar. There were 200 aggregate spherical grains (diameter range 2 - 16 mm) and 8,000 mortar spherical grains (diameter range 0.25 - 2 mm).

2 CONTACT LAWS FOR THE DEM MODELS

DI and DII were derived from a family of discrete element (DEM) models of fracture in concrete, previously reported in (Nitka and Tejchman, 2015; Skarżyński et al., 2015; Suchorzewski et al., 2018a,b): readers are referred to these papers for full details including model calibration on laboratory tests on real concrete specimens. Here, we elaborate below on the contact models used since the contacts and their capacities form an input to the network flow analysis. The DEM model takes advantage of the so-called soft-particle approach (i.e. the model allows for grain deformation that is modelled as an overlap of grains) (Fig.1, Eqns. 1-6 in (Nitka and Tejchman, 2015)). The interaction force vector representing the action between two spherical discrete elements in contact was decomposed into a normal and tangential vector, respectively (Fig. 1(A) and 1(B) in (Nitka and Tejchman, 2015)). A linear normal contact model under compression was used (Fig. 1(B) in (Nitka and Tejchman, 2015)). The normal forces acting on spheres were modelled by an elastic law with cohesion. The normal and tangential forces were linked to the displacements through the normal stiffness and the tangential stiffness. These stiffness values were computed as functions of: the modulus of elasticity of the grain contact and the radii of the grains in contact for the normal stiffness, and the modulus of elasticity, Poisson's ratio of the grain contact, and the radii of the grains in contact for the tangential stiffness (Eqn. 3 in (Nitka and Tejchman, 2015)). The unloading was purely elastic (Fig.1(C) in (Nitka and Tejchman, 2015)).

The tangential and normal forces at a contact were coupled together by the cohesive-frictional Mohr-Coulomb equation (Fig. 1(D), Eqn. 4 in (Nitka and Tejchman, 2015)). The cohesive force and tensile force were assumed as a function of the cohesive stress (maximum shear stress at pressure equal to zero), tensile

normal stress and sphere radius (Eqn. 5 in (Nitka and Tejchman, 2015)). Of relevance to this analysis is the normal force during tension: in this case, the normal force may be negative down to the minimum value $F^n_{min} = T(r^2_{min})$ where T is the minimum tensile normal stress and r_{min} is the radius of the smaller grain for the pair of grains in contact. If this minimum normal force was reached, the contact was broken.

For DI, the contact properties were as follows. For all grain-grain contacts, the modulus of elasticity $E_c = 15$ GPa, Poisson's ratio $\nu_c = 0.2$, cohesion $C = 140$ MPa and minimum tensile stress $T = 25$ MPa. The grain-grain friction angle was $\mu = 30°$, the mass density $\rho = 2500$ kg/m^3 and the damping parameter $\alpha_d = 0.08$.

For DII, the contact properties were as follows. For the cement-cement contacts, we assume: modulus of elasticity $E_c = 11.2$ GPa, Poisson's ratio $\nu_c = 0.2$, cohesion $C = 140$ MPa and minimum tensile stress $T = 24.5$ MPa. For the cement-aggregate(ITZ) contacts, we assume: modulus of elasticity $E_c = 7.8$ GPa, Poisson's ratio $\nu_c = 0.2$, cohesion $C = 100$ MPa and minimum tensile stress $T = 17.5$ MPa. The grain-grain friction angle was $\mu = 18°$, the mass density $\rho = 2500$ kg/m^3 and the damping parameter $\alpha_d = 0.08$.

3 METHOD FOR IDENTIFICATION OF TENSILE FORCE CHAINS

Tensile force chains carry the majority of the tensile load in the sample. Following the method used to identify compressive force chains in (Muthuswamy and Tordesillas, 2006), identifying tensile force chains from data on contact forces proceeds in two steps.

- *Step 1 of 2: Find the particle load vector and type of each particle.*
  The *particle load vector* $\mathbf{P}$, is derived from the local force moment tensor associated with each particle, defined as

$$\hat{\sigma}_{ij} = \sum_{c=1}^{N} {f_i}^c {r_j}^c, \tag{S1}$$

  where N is the number of contacting neighbors of the particle (or grain), ${f_i}^c$ denotes the components of the contact force, and ${r_j}^c$ denotes the components of the unit normal vector from the center of the particle to the point of contact (Peters et al., 2005). The magnitude and direction of the particle load vector $\mathbf{P}$ is given by the largest eigenvalue of $\hat{\sigma}_{ij}$ and its corresponding eigenvector. If the tensile (compressive) forces acting on the particle are dominant, the sign of the largest eigenvalue will be positive (negative) and we classify the particle as $\mathrm{T_e}$ (C_o). We group all $\mathrm{T_e}$ grains in one class and call it the $\mathrm{T_e}$-class.
- *Step 2 of 2: Identify tensile force chains in the T_e-class.*
  A tensile force chain is defined as a chain of three or more $\mathrm{T_e}$ particles in contact, whose particle load vector magnitudes each exceed the global average value in the $\mathrm{T_e}$-class and whose particle load vectors are in alignment with each other to within a prescribed tolerance angle θ, that is

$$\cos\theta < \frac{\mathbf{P}\cdot\mathbf{l}_c}{|\mathbf{P}|\,|\mathbf{l}_c|} \leq 1, \tag{S2}$$

  where $\mathbf{l}_c$ is the branch vector from the center of the focal particle to its neighbor in the tensile force chain. Further details concerning this algorithm can be found in (Muthuswamy and Tordesillas, 2006).

3.1 Spatial evolution of force chains in DI and DII

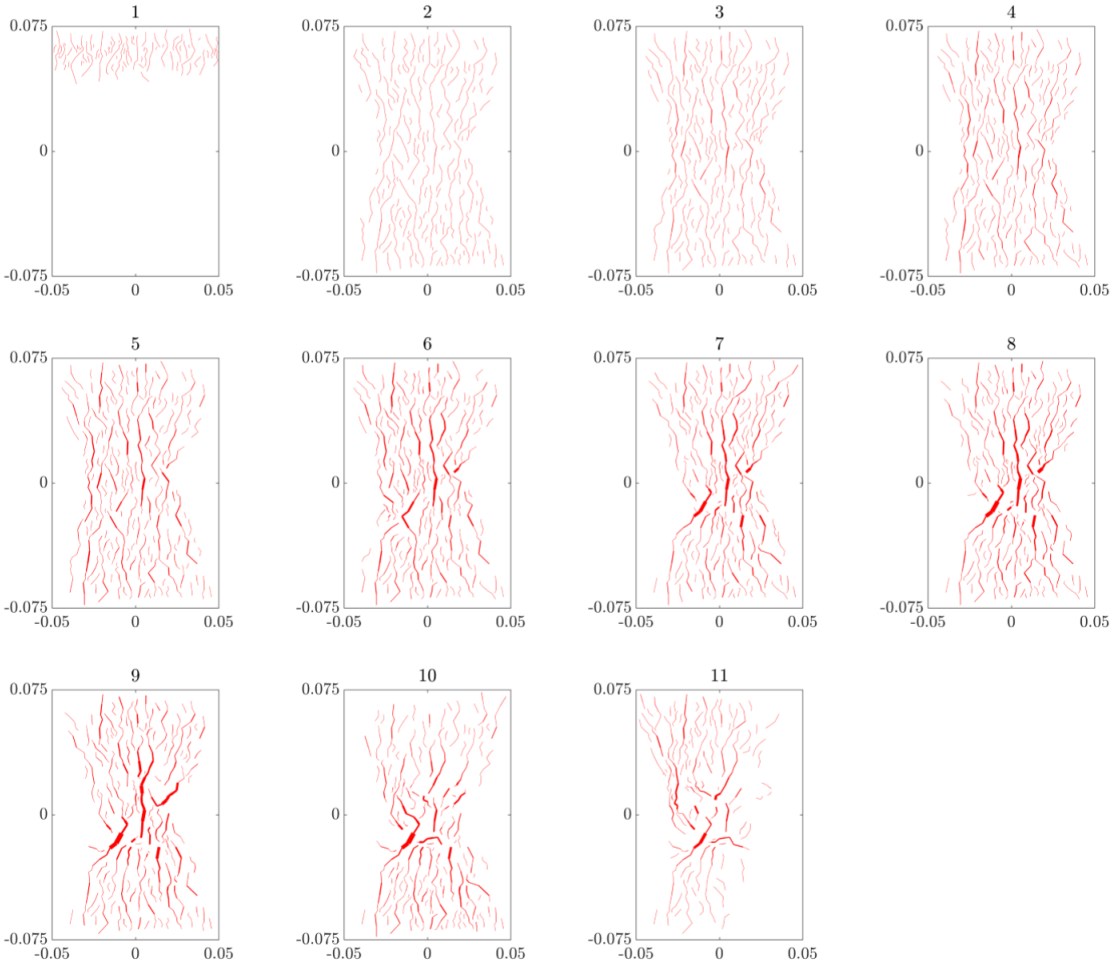

Figure S1. *DI: Force transmission is governed by tensile force chains.* The spatial distribution of tensile force chains is visualized here by the contact links (lines connecting the centroids of grains in the chain): link thickness is proportional to the magnitude of the tensile force transmitted at the contact. A percolating tensile force chain network is first established at stage 2.

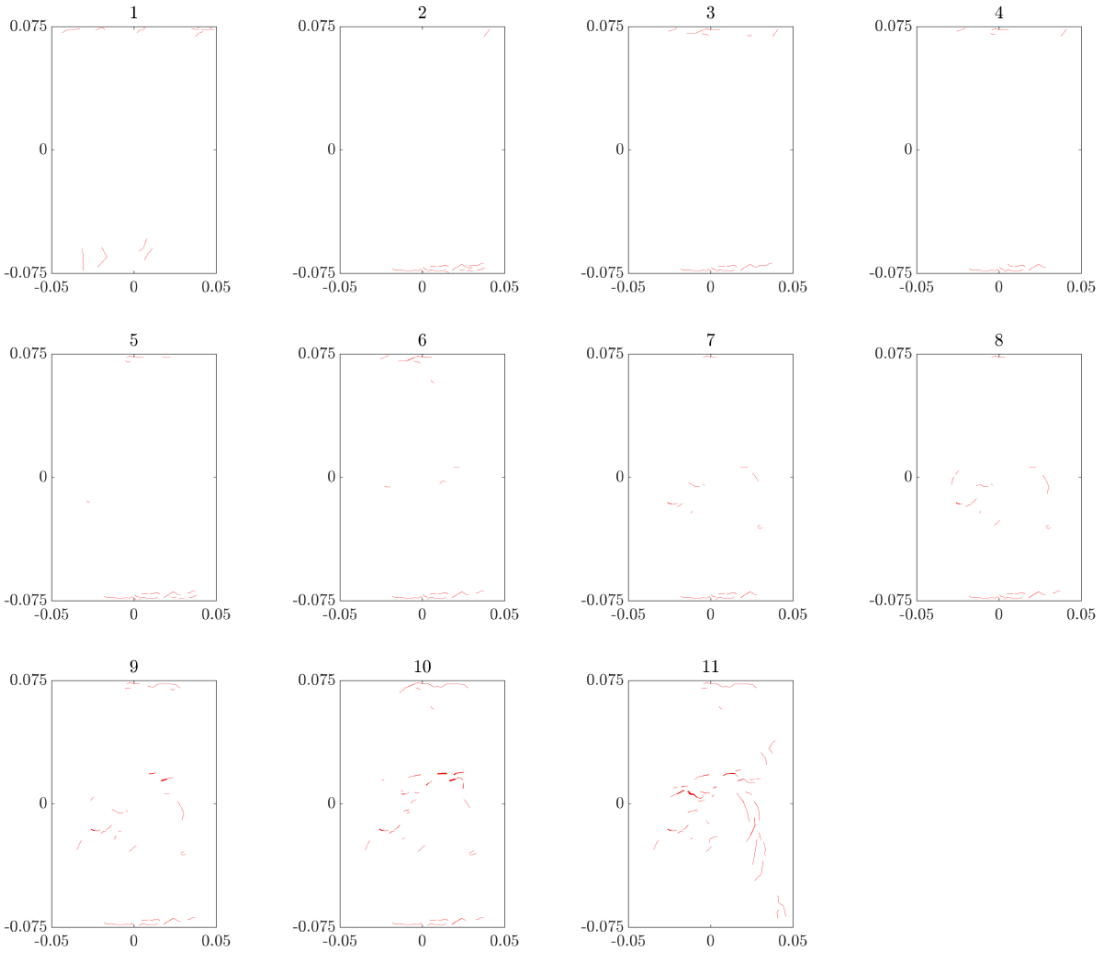

Figure S2. *DI: A negligible number of compressive force chains form in the pre-failure regime.* The spatial distribution of compressive force chains is visualized here by the contact links (lines connecting the centroids of grains in the chain): link thickness is proportional to the magnitude of the compressive force transmitted at the contact using the same scale as that used to visualize the tensile force chains in Figure S1 to allow direct comparison.

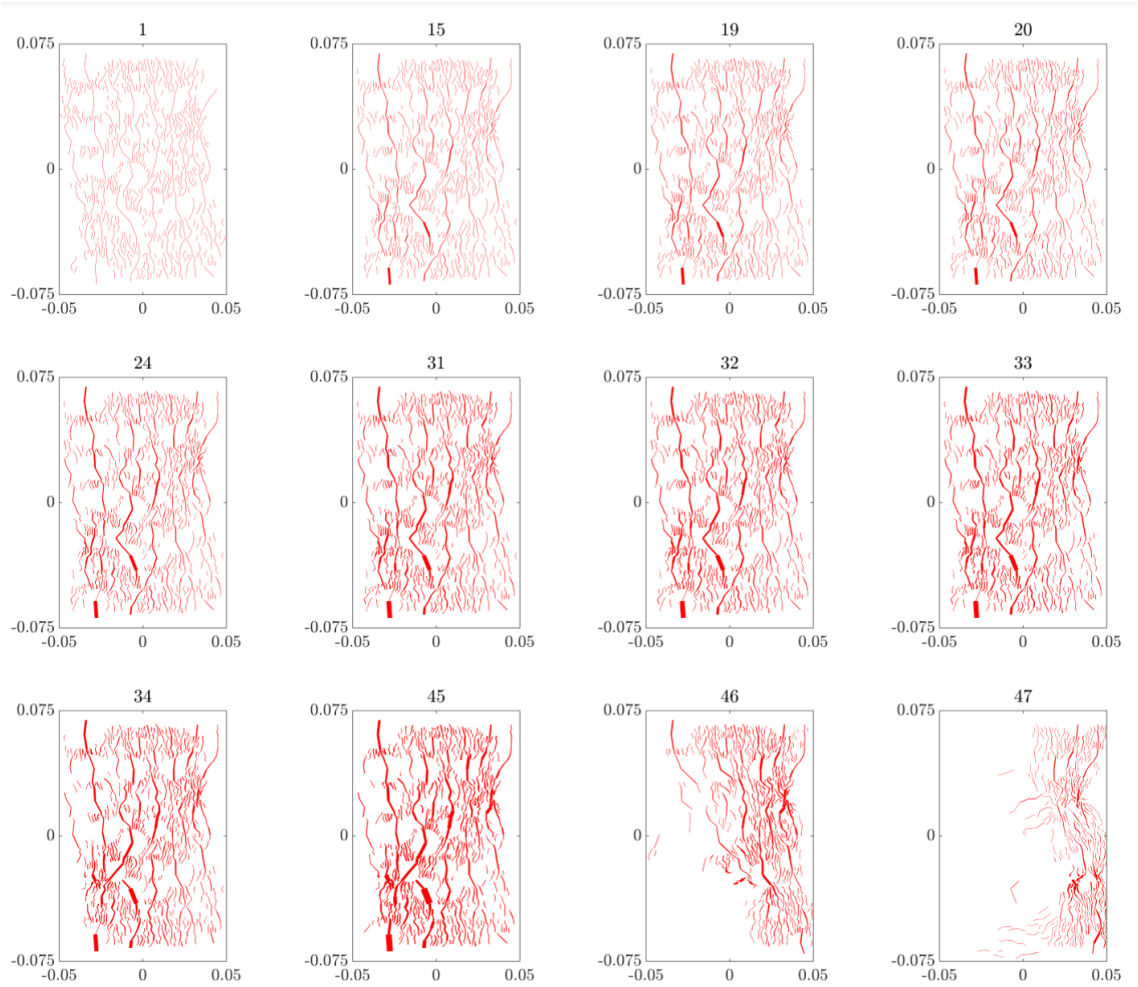

Figure S3. *DII: Force transmission is governed by tensile force chains.* The spatial distribution of tensile force chains at key stages is visualized here by the contact links (lines connecting the centroids of grains in the chain): link thickness is proportional to the magnitude of the tensile force transmitted at the contact. A percolating tensile force chain network is first established at stage 1.

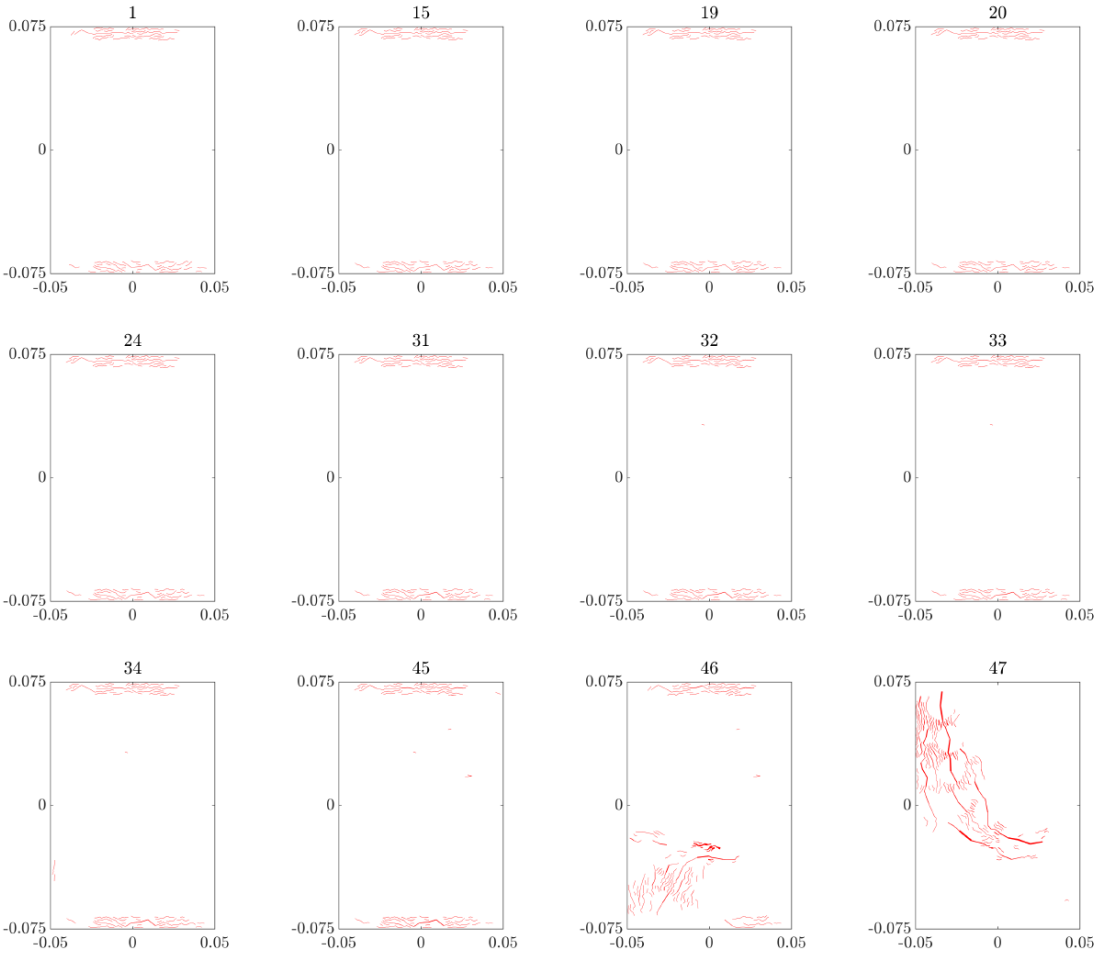

Figure S4. *DII: A negligible number of compressive force chains form in the pre-failure regime.* The spatial distribution of compressive force chains at key stages is visualized here by the contact links (lines connecting the centroids of grains in the chain): link thickness is proportional to the magnitude of the compressive force transmitted at the contact using the same scale as that used to visualize the tensile force chains in Figure S3 to allow direct comparison.

4 FORCE FLOW CAPACITY INDEX

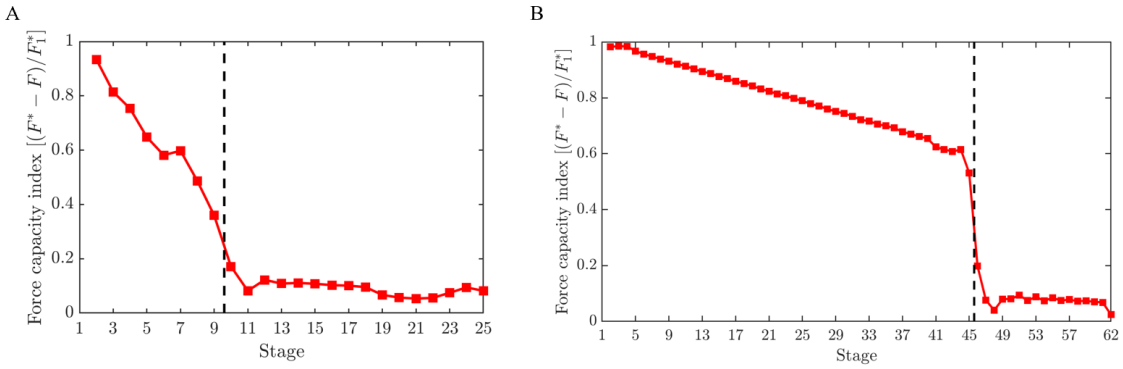

Figure S5. (Color online) *Force flow capacity index* $\eta = (F^* - F)/F_1^* \to 0$*, as indicator of failure.* (A) DI and (B) DII. Note that there are still bonded contacts that remain in the final time state, hence neither sample has completely split up into two pieces. Additional time steps in the failure regime are included to show limit behavior.

5 MOST TENSILE FORCE CHAIN LINKS ARE IN $\mathcal{P}$

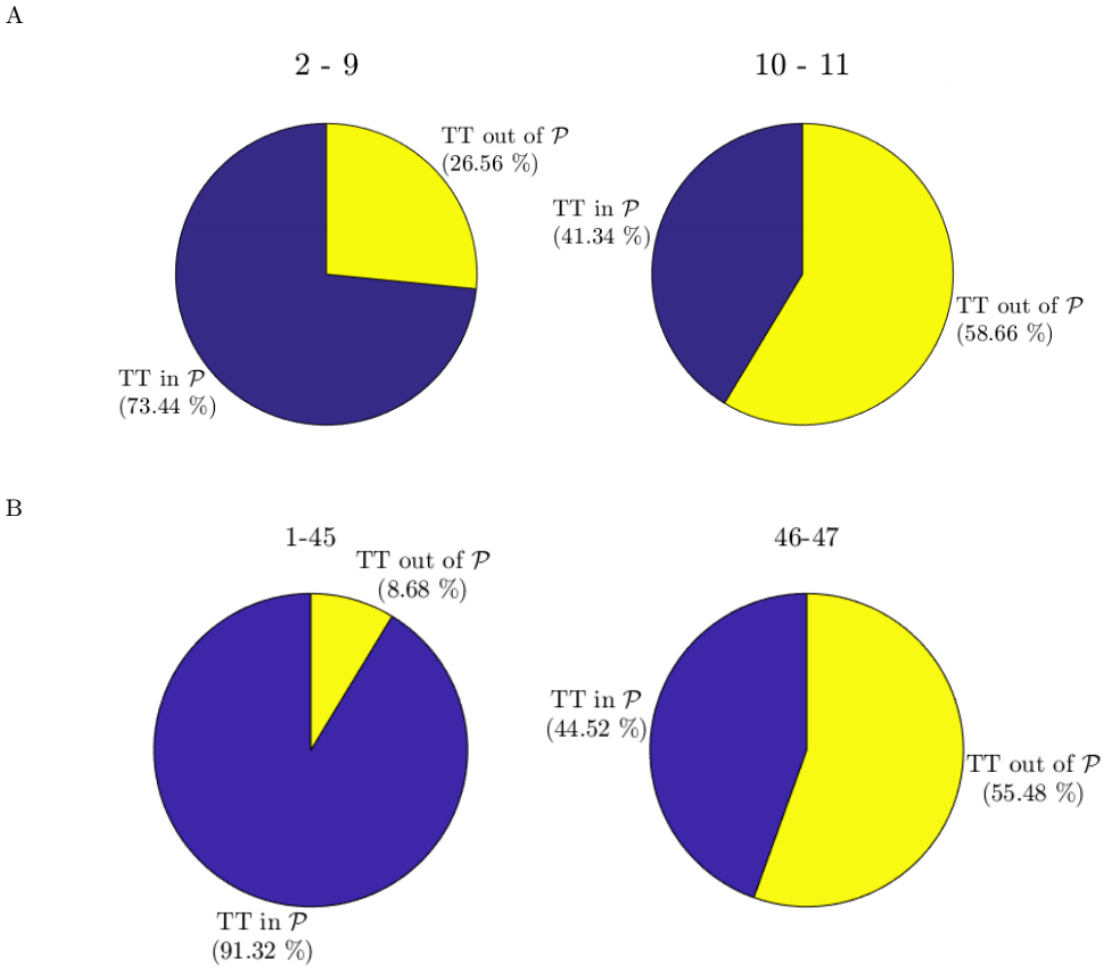

Figure S6. (Color online) *Most tensile force chain links (TT) are in $\mathcal{P}$ in the pre-failure regime.* Percentage population of TT links in versus out of $\mathcal{P}$, averaged over (A) the pre-failure (stages $2-9$) and post-failure (stages $10-11$) regimes for DI and (B) the pre-failure (stages $1-45$) and post-failure (stages $46-47$) regimes for DII.

6 SPATIAL DISTRIBUTION OF FORCE BOTTLENECKS IN DI AND DII

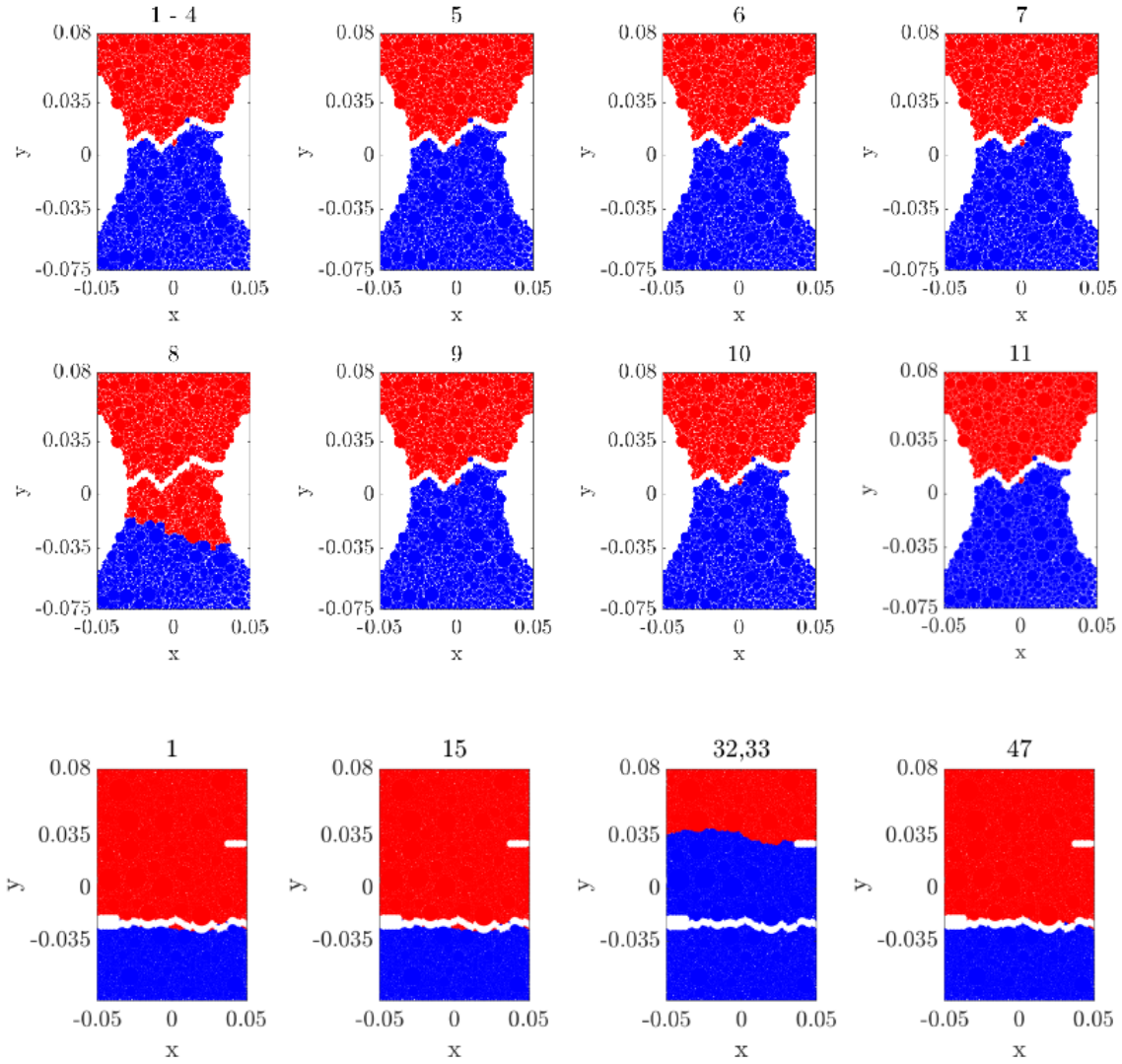

Figure S7. (Color online) *Force bottlenecks B provide an early prediction of the ultimate crack pattern* . Spatial distribution of the bottlenecks B for (A) DI and (B) DII. Grains on either side of the ultimate macrocrack are artificially separated to aid visual comparison of the bottleneck versus the actual macrocrack location. Prediction persists for all stages except stage 8 (stages 32, 33) for DI and DII respectively, where it predicts the secondary or competing bottleneck. Stage corresponds to the peak force in between stages 9 and 10 (45 and 46) for DI and DII respectively. Note also that for DII we have only included predictions for selected stages. Other stages have similar predictions.

7 QUANTIFYING THE ERROR OF PREDICTION OF MACROCRACK LOCATION

Here we quantify the error between the predicted location and the actual location of the macrocrack. The percentage error of prediction of macrocrack location is given by

$$P_e = \frac{|(V_{B_u} \setminus V_{C_u}) \cup (V_{C_u} \setminus V_{B_u})|}{|V_T|} \times 100, \tag{S3}$$

where V_{B_u}, V_{C_u} are the grains in the upper part of bottleneck and upper part of macrocrack respectively, V_T is all the grains in the sample, and $|\ \ |$ denotes the cardinality (size = number of grains). This quantifies the number of offset grains (i.e., red colour grains below and blue colour grains above the separation as shown in Figure S7) in the prediction relative to macrocrak normalized to the total number of grains. If the grains are in the upper part of the prediction and upper part of the macrocrack is identical, the percentage error is 0. In other words, if the red-blue interface of Figure S7 is same as the artificial separation (i.e., no red colour grains below and no blue colour grains above the separation), then the percentage error is 0. Otherwise, we have non zero error. As can be seen from Figure S8, the error of prediction of macrocrack location by B^* is less than 1%, except when the secondary bottleneck appears in stage 8 for D1 and stages 32-33 for DII.

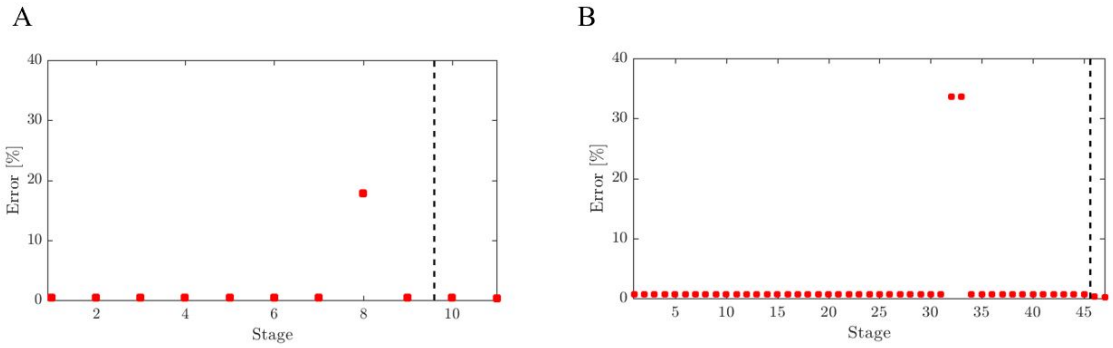

Figure S8. (Color online) *The error of prediction of macrocrack location by B^* is less than 1%, except when the secondary bottleneck appears in stage 8 for D1 and stages 32-33 for DII.* Evolution of the percentage error of prediction of macrocrack location given by Equation S3 for (A) DI and (B) DII.

REFERENCES

Muthuswamy, M. and Tordesillas, A. (2006). How do interparticle contact friction, packing density and degree of polydispersity affect force propagation in particulate assemblies? *Journal of Statistical Mechanics: Theory and Experiment* 2006, P09003

Nitka, M. and Tejchman, J. (2015). Modelling of concrete behaviour in uniaxial compression and tension with DEM. *Granular Matter* 17, 145–164

Peters, J., Muthuswamy, M., Wibowo, J., and Tordesillas, A. (2005). Characterization of force chains in granular material. *Physical Review E* 72, 041307

Skarżyński, Ł., Nitka, M., and Tejchman, J. (2015). Modelling of concrete fracture at aggregate level using FEM and DEM based on X-ray μCT images of internal structure. *Engineering Fracture Mechanics* 147, 13–35

Suchorzewski, J., Tejchman, J., and Nitka, M. (2018a). Discrete element method simulations of fracture in concrete under uniaxial compression based on its real internal structure. *International Journal of Damage Mechanics* 27, 578–607

Suchorzewski, J., Tejchman, J., and Nitka, M. (2018b). Experimental and numerical investigations of concrete behaviour at meso-level during quasi-static splitting tension. *Theoretical and Applied Fracture Mechanics* 96, 720–739

Van Vliet, M. R. and Van Mier, J. G. (1999). Effect of strain gradients on the size effect of concrete in uniaxial tension. In *Fracture Scaling* (Springer). 195–219